analytical chemistry

Article

Detection of SARS-CoV-2 DNA Targets Using Femtoliter Optofluidic Waveguides

Megan Makela and Pao Tai Lin*

Read Online

ACCESS | Metrics & More | Article Recommendations

ABSTRACT: Chip-scale SARS-CoV-2 testing was demonstrated using silicon nitride (Si_3N_4) nanoslot fluidic waveguides to detect a tagged oligonucleotide with a coronavirus DNA sequence. The slot waveguides were fabricated using complementary metal−oxide−semiconductor (CMOS) fabrication processes, including multiscale lithography and selective reactive ion etching (RIE), forming femtoliter fluidic channels. Finite difference method (FDM) simulation was used to calculate the optical field distribution of the waveguide mode when the waveguide sensor was excited by transverse electric (TE) and transverse magnetic (TM) polarized light. For the TE polarization, a strong optical field was created in the slot region and its field intensity was 14× stronger than the evanescent sensing field from the TM polarization. The nanoscale confinement of the optical sensing field significantly enhanced the light−analyte interaction and improved the optical sensitivity. The sensitivity enhancement was experimentally demonstrated by measuring the polarization-dependent fluorescence emission from the tagged oligonucleotide. The photonic chips consisting of femtoliter Si_3N_4 waveguides provide a low-cost and high throughput platform for real-time virus identification, which is critical for point-of-care (PoC) diagnostic applications.
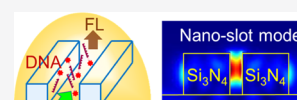
The coronavirus disease 2019 (COVID-19), caused by an infection of the severe acute respiratory syndrome coronavirus 2 (SARS-CoV-2), spread throughout the world, posing unprecedented challenges to public health.[1] The World Health Organization (WHO) declared COVID-19 as a public health emergency of international concern[2] because the virus spread to 188 countries and territories with over 5.31 million infections and over 333,000 deaths reported worldwide as of May 23, 2020.[3] Epidemic episodes such as the ongoing COVID-19 pandemic and other outbreaks such as Zika virus in 2015−2016,[4] Ebola virus in 2013−2016,[5] nd Influenza A/H1N1 virus in 2009−2010[6] have happened regularly throughout the last decade. Henceforth, screening and making accurate and timely diagnoses of large numbers of possibly infected individuals are critical to contain such outbreaks effectively.[7−9] The current gold standard of testing for viral diseases such as COVID-19 is real-time quantitative polymerase chain reaction (qPCR),[10,11] which can detect both infections in their early stage and asymptomatic cases. However, the availability and the capacity to perform the qPCR tests in a timely manner is a huge limitation of testing-based mitigation strategies. On the other hand, point-of-care (PoC) diagnostic devices are platforms designed to be cost-efficient, portable, and simple to operate, with high accuracy and specificity compared to their traditional laboratory counterparts.

Among various PoC technologies, optical waveguides are an ideal platform for rapid and sensitive biomolecule detection. Applying the evanescent field from waveguides, photonic biosensors become extremely versatile and can been applied through a variety of detection methods, including refractom-

etry, absorption, emission, and fluorescence.[12−15] In addition, many materials used for creating waveguides are compatible with existing complementary metal−oxide−semiconductor (CMOS) fabrication processes so that manufacturing is highly scalable.[16] A conventional optical waveguide is made by a high refractive index core and a low refractive index substrate or cladding, and thus the optical field is mainly confined inside the waveguide.[17] However, to attain high sensitivity, it is desired to have a waveguide structure creating a stronger evanescent field. This can be achieved by a nanoslot component that creates a strong light confinement within the slot region that also serves as a fluidic channel.[18] The enhanced optical field overlaps with the fluidic slot channel and results in a stronger interaction between the light and the analyte and thus enhances sensitivity.[19,20] In addition, devices consisting of nanoslot waveguides allow for high-volume CMOS manufacturing and further integration with other microphotonic components.

This work developed a slot waveguide with a femtoliter fluidic channel to test the SARS-CoV-2 genetic material. The design of the nanoslot structure and the calculation of the waveguide mode profiles were performed by using the two-dimensional finite difference method (FDM). Enhancement of
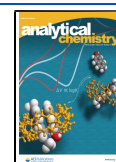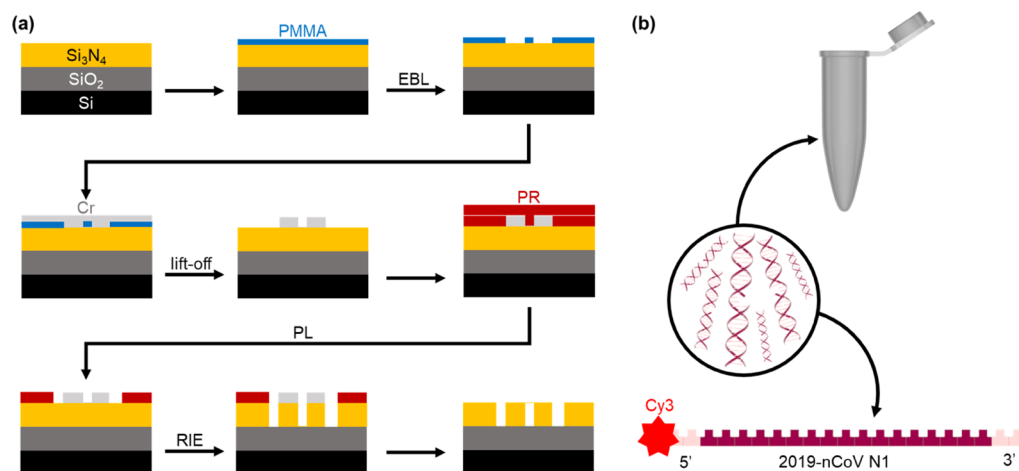
Figure 1. (a) Fabrication processes of the optofluidic sensors with Si_3N_4 nanoslot waveguides. Si_3N_4 thin film was deposited on a Si wafer via PECVD, and the nanoslot components were patterned by EBL. A Cr mask layer was deposited on the device using e-beam evaporation, and the excess Cr was lifted off by acetone. Positive tone PR was then spun on the device, where the input and output waveguides were defined using PL. The patterns were transferred to the Si_3N_4 layer through RIE. Afterward, the mask materials were removed with a stripper and an etchant. (b) Details of the oligonucleotide, a single strand 2019-nCoV N1 marker modified with a Cy3 fluorescent probe molecule.

the optical sensitivity was experimentally characterized by measuring the polarization-dependent fluorescence spectra from the tagged SARS-CoV-2 sequence. The methodology of the optofluidic waveguide sensing can also be applied to test recurrent disease outbreaks such as malaria,[21] dengue fever,[22] and measles[23] to advance the PoC diagnostic technologies.

■ METHODS

Device Fabrication. Multistep fabrication processes including thin film deposition, lithography, and selective plasma etching were used to fabricate the Si_3N_4 nanoslot waveguides and the input and output strip waveguides. The detailed process is illustrated in Figure 1a. The devices were fabricated on a 525 μm thick Si wafer substrate with a 3 μm thick plasma-enhanced chemical vapor deposition (PECVD) SiO_2 layer. A 400 nm layer of Si_3N_4 was then deposited by PECVD using dilute SiH_4 and N_2 precursor gases at a temperature of 350 °C. PECVD is a lower temperature deposition process compared to LPCVD operated at 700–800°. Therefore, fabricating SiN waveguides through PECVD has better capability for integration with other optical devices and materials.[24,25] A double layer of 495 and 950 K PMMA A4 positive electron beam resists were spun onto the substrate, and the nanoslot waveguide patterns were generated using electron beam lithography (EBL). Then, a 50 nm Cr mask layer was deposited using electron beam evaporation, followed by the lift-off process. The device was then spin-coated with an S1818 photoresist (PR) to create patterns of the input and output waveguides that were aligned to the EBL-defined nanoslot pattern through photolithography (PL). The device patterns were transferred into the Si_3N_4 layer by plasma etching. Reactive ion etching (RIE) with SF_6 and Ar etching gases were used to create smooth sidewalls and reduce the waveguide propagation losses.[26,27] Finally, the Cr mask and PR were removed using a ceric ammonium nitrate etchant solution and 1-methyl-2-pyrrolidon (NMP)-based remover, respectively. The final structure consisted of 400 nm tall slot waveguides, tapered couplers, and input and output strip waveguides.

Sample Preparation. The sequence of the DNA sample utilized in the measurements is

5'-/Cy3/GGT CCA AAC GTA ATG CGG GGT-3′
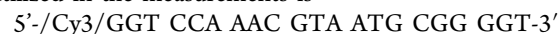
This synthetic oligonucleotide is an exact sequence match to the cDNA product synthesized using a standard reverse transcription (RT) protocol on a SARS-CoV-2 viral RNA target. In particular, this transcript corresponds to a target region ("N1") on the nucleocapsid (N) gene of the SARS-CoV-2 genome, selected by the U.S. Centers for Disease Control and Prevention (CDC), Division of Viral Diseases, for use with conventional nucleic acid diagnostic methods.[28] It has been successfully applied in molecular assays to detect SARS-CoV-2 nucleic acid in the respiratory specimens from COVID-19 suspected individuals.[29] Labeled oligonucleotides, with their structure depicted in Figure 1b, were purchased from Integrated DNA Technologies (IDT). A 100 μM solution of DNA with Cy3 marker was diluted in sterilized water to a 10 μM final concentration to be used as the analyte.

Test System Setup. Figure 2a illustrates the schematic of the test system used to measure the fluorescence spectrum from the tagged DNA. The excitation light source was a diode-pumped solid-state green laser with the output centered at λ = 532 nm and a maximum power of 1 W. The excitation light was collimated into a single mode silica fiber with a 3.5 μm core using a reflective collimator (RC). A $\lambda/2$ phase retarder was placed before the collimator to enable the polarization rotation of the linearly polarized laser light. The fiber was butt-coupled into the Si_3N_4 waveguide next to its cleaved front facet using highly accurate three-axis micropositioning stages. The alignment was monitored by an overhead microscope with a long-working distance objective. As shown in Figure 2b, after the alignment, strong guided light was observed over the entire length of the device, including both the strip and nanoslot waveguide regions. To perform the measurements, 1 μL of the analyte was pipetted directly onto the surface of the waveguide device, such that the entire slot waveguide region was wetted by the sample. Fluorescence emitted from the labeled DNA and excited by the guided green light was collected from the waveguide surface by a 50 μm core multimode silica fiber connected to a compact CCD spectrometer (Thorlabs). Positioning of the probe fiber was controlled by precision
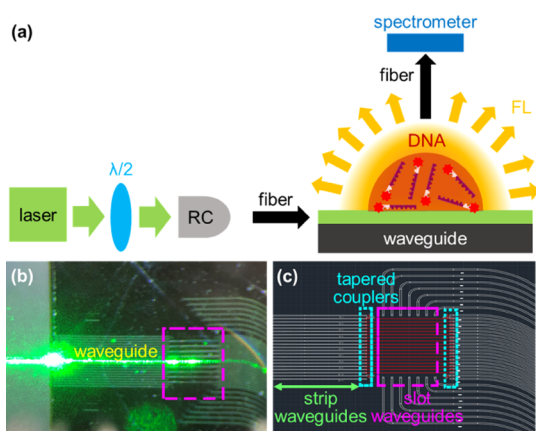
Figure 2. (a) Schematic of the measurement test system. Light from a 532 nm laser was passed through a $\lambda/2$ phase retarder and coupled into a fiber using a RC. The fiber is butt-coupled to the cleaved facet of the waveguide device. Fluorescence emission (FL) from the Cy3-modified DNA is collected through a fiber to a spectrometer. (b) Image of fiber-chip coupling via an overhead microscope. (c) Schematic of the complete device structures, with taper couplers highlighted in blue and nanoslot waveguides in pink.
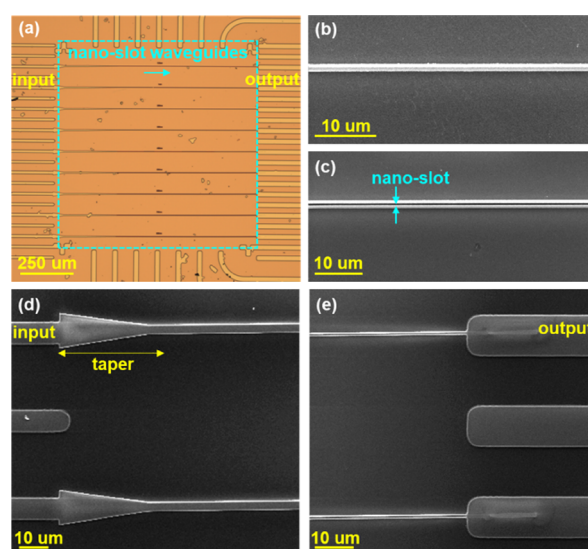

Figure 3. (a) Optical image of a nanoslot waveguide array connected with input and output waveguides. The SEM images of (b) strip waveguide, (c) nanoslot waveguide, (d) input waveguides with tapers, and (e) output waveguides. The nanoslot structures were defined by EBL, while the input and output portions were patterned by PL.

alignment stages that optimized the collection efficiency of the fluorescence signal. Deionized water was used to rinse between measurements. The removal of previous substances from the device surface was verified by a spectrometer and compared to a background spectrum taken at the start of the experiment. Spectra were acquired using the Thorlabs OSA software using a 1000 ms integration time. Analysis of the recorded signals was performed by Origin (OriginLab) software. Figure 2c is the schematic showing details of the device structures. A mode converter consisting of a taper structure and a strip waveguide was created between the input fiber and the slot waveguide. The converter can efficiently reduce the transmission loss caused by the mode mismatching between the fiber and the slot waveguide.[30,31]

RESULTS AND DISCUSSION

Device Structure Characterization. The morphology of the fabricated slot waveguide devices was inspected using optical microscopy and scanning electron microscopy (SEM). Figure 3a shows the optical image of an array of the input and output strip waveguides and the nanoslot waveguides in the center of the devices. The structures are clearly defined with a smooth top surface, indicating uniform etching with no damage introduced during the RIE process. Figure 3b,c shows enlarged images of the reference strip waveguides and the nanoslot waveguides, respectively. The strip waveguide in Figure 3b has a width of 0.8 μm. From Figure 3c, it can be seen that the nanoslot waveguide has a slot width of d = 100 nm centered between two 0.4 μm wide Si_3N_4 strips. Figure 3d shows a higher magnification image of the input region that has a taper structure. Figure 3e shows the output region highlighting the transition from the nanoslot waveguide to a wider output waveguide. The accurate alignment between the slot waveguide and the input and output waveguides and the taper coupler ensured the efficient excitation of nanoslot waveguide mode.

Optical Waveguide Simulation. The sensitivity of the nanoslot waveguides and their counterpart strip waveguide was first evaluated using two-dimensional FDM. The sensitivity

enhancement was then determined by comparing the optical fields from these waveguides. The device dimensions used in the simulations were based on the SEM images shown in Figure 3. $n_{Si_3N_4}$ = 2.10 and n_{SiO_2} = 1.45 were the refractive indices of the waveguide core and undercladding material, respectively. A 2 μm × 0.8 μm excitation source at λ = 532 nm was selected. Figure 4a illustrates the structure of an 800 nm
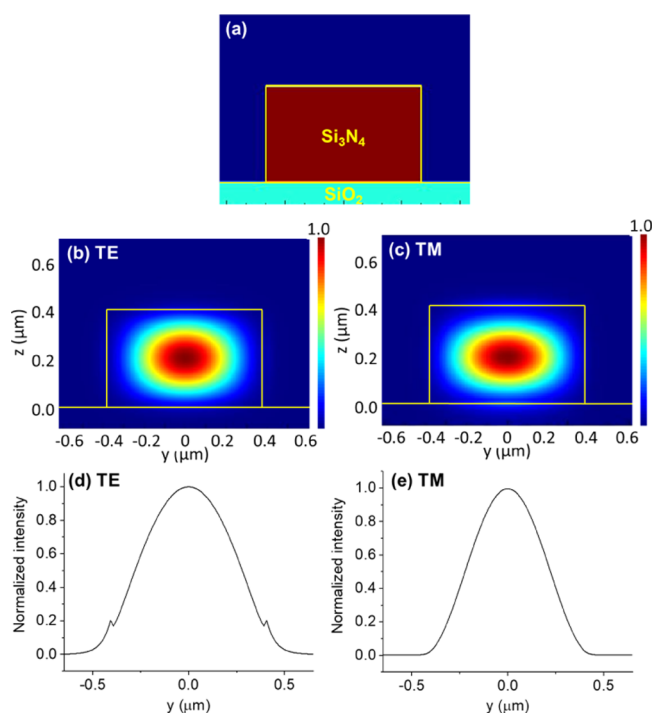

Figure 4. (a) Structure of a strip waveguide used in the FDM modeling. (b) Waveguide modes excited by (b) TE- and (c) TM-polarized light, respectively. 1D intensity profiles of the (d) TE and (e) TM modes taken along the y-axis at a height of z = 200 nm.

wide strip waveguide used in the simulation. For both transverse electric (TE) and transverse magnetic (TM) polarized light, an elliptical fundamental mode was obtained at the center of waveguide as depicted in Figure 4b,c. The corresponding one-dimensional profiles of their field distribution taken along the y-axis are plotted in Figure 4d,e, where nearly all of the light was contained inside the Si_3N_4 strip. Examining the field distribution, TE-polarized waveguide mode only has 3.4% of its intensity belonging to the evanescent wave. An even smaller portion of 0.2% was found for the TM polarized waveguide mode. Therefore, the optical field was mainly confined in the center of a conventional strip waveguide, where the evanescent field extending outside the waveguide was very weak. Further reducing the thickness and width of the strip waveguide will decrease the coupling efficiency between the input fiber and the waveguide.

The same simulation approach was applied to analyze the waveguide mode and field distribution of the nanoslot waveguide shown in Figure 5a. The nanoslot waveguide
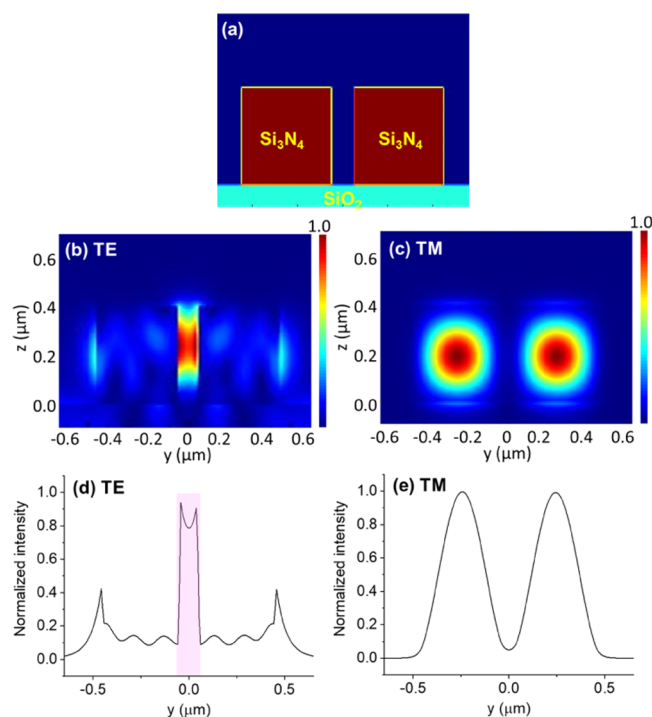

Figure 5. (a) Structure of a nanoslot waveguide used in the FDM modeling. (b) Waveguide modes excited by (b) TE and (c) TM polarized light, respectively. 1D intensity profiles of the (d) TE and (e) TM modes taken along the y-axis, at a height of z = 200 nm. Unlike a strip waveguide with the mode inside the Si_3N_4 region, a nanoslot waveguide had the light confined in the slot region that overlapped with the fluidic channel highlighted by pink.

consisted of two 400 nm wide Si_3N_4 strips separated by a 100 nm gap. An even narrower gap will cause a larger propagation loss due to surface scattering. For TE polarization, depicted in Figure 5b, the field was highly concentrated in the center of the 100 nm nanoslot region, which also served as the fluidic channel to be filled with the analyte. On the other hand, for the TM polarized light shown in Figure 5c, only a small portion of the field extended outside of the Si_3N_4 strips. The one-dimensional field distribution of the TE and TM waveguide modes are plotted in Figure 5d,e, respectively. For TE-

polarized mode, the nanoslot waveguide had a significantly high optical field with 50.5% of the light intensity confined in the slot region. In contrast, for the TM mode, the portion of the field extending outside of the Si_3N_4 strips was merely 5.9%, which was similar to the TM mode of a single strip waveguide shown in Figure 4e. Compared to the counterpart single strip waveguide, the TE mode of the nanoslot waveguide revealed a 14× enhancement of the optical intensity. The direct overlap between the fluidic channel and the waveguide mode, plus the enhanced excitation light intensity, significantly improved the overall sensitivity due to the increased light−analyte interaction. Unlike other methods that improve the optical sensitivity by decreasing the waveguide thickness, our approach converted a guided lightwave into a nanoscale optical probe without a reduction in coupling efficiency or increase in the optical loss. Thus, the nanoslot waveguide device provided an advantageous platform for the sensing of genetic materials.

SARS-CoV-2 Sensing. The sensing capability and sensitivity improvement of the nanoslot waveguide devices were evaluated. The analyte was a SARS-CoV-2 cDNA oligo with Cy3 fluorescent tag, a positive control representing the product of a standard RT protocol on a sample containing the CDC-identified SARS-CoV-2 viral target. The fluorescence of the analyte was excited by the waveguide devices. Cyanine 3 dye or Cy3 is a synthetic dye molecule commonly used for labeling and quantification of nucleic acids or protein molecules. Cy3 is a yellow−orange fluorescent molecule that can be excited by the 488 or 532 nm laser lines. The wavelength for maximum excitation is 555 nm, and its strongest emission is near 565 nm.[32] A negative control sample, representing a cDNA product generated from a standard RT protocol on a specimen not containing the SARS-CoV-2 viral RNA target, was also tested for comparison. This oligonucleotide analyte contains cDNA produced from the single-stranded RNA virus *Dengue virus*, serotype 1 (DENV1, 5′-GTACCCTGGTGGTAAGGACT-3′). Figure 6a shows the emission spectra of the Cy3-labeled SARS-CoV-2 oligo when it was excited by the slot Si_3N_4 waveguide at λ = 532 nm, and the dashed line shows the emission spectrum of the DENV1 negative control yielding no fluorescence. Additionally, the obtained emission spectrum of the SARS-CoV-2 oligo shows identical spectral features when excited by the laser alone applying the waveguide device. This indicates that the Si_3N_4 did not cause unwanted luminescence background or otherwise alter the emission spectra of the genetic analyte.

To investigate the polarization-dependent sensing performance of the nanoslot waveguides, a $\lambda/2$ phase retarder was added into the system to rotate the polarization of the input laser light, thus enabling the excitation of both TE and TM waveguide modes. The ratio of the TE/TM components was adjusted by rotating the phase retarder at different angles, $\boldsymbol{\theta}$. At $\boldsymbol{\theta}$ = 0°, the waveguide mode was TE-polarized, whereas at $\boldsymbol{\theta}$ = 45°, it was TM-polarized. Figure 6a displays the emission spectra of the DNA analyte, as the $\boldsymbol{\theta}$ increased from 0, 10, 20, 30, to 40°. The fluorescence emission was strongest at $\boldsymbol{\theta}$ = 0° because the waveguide mode was converted from TE to TM polarization. The inset displays emission intensities as the oligo concentration ranges from 1 to 10 μM. The intensity versus concentration plot has a similar variation at different emission wavelengths. Figure 6b displays the measured fluorescence intensity-polarized light excited the nanoslot waveguide mode. The emission intensity gradually dropped as the $\boldsymbol{\theta}$ increased at the emission maximum λ = 565 nm. The intensity dropped
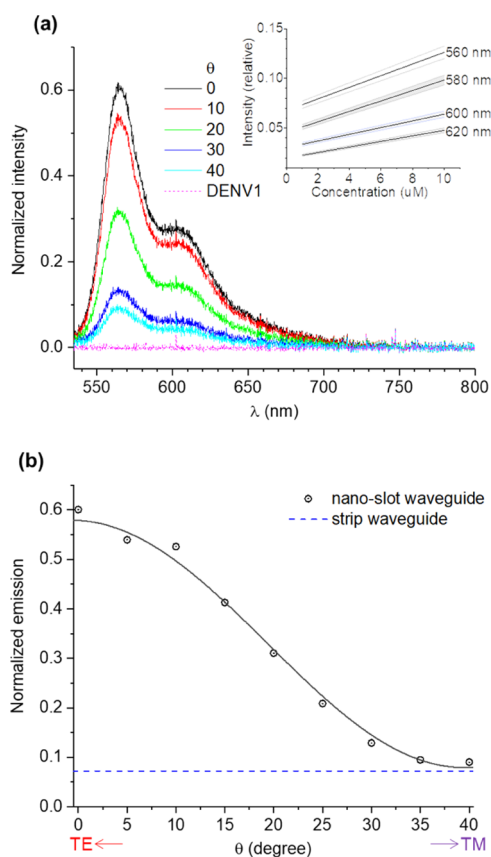
Figure 6. (a) Emission spectra of SARS-CoV-2 cDNA and DENV1 cDNA excited by a nanoslot waveguide with different polarized light. The light polarization was controlled by a $\lambda/2$ phase retarder with various rotation angle θ. The inset shows the concentration plots at emission wavelengths of 560, 580, 600, and 620 nm, and their corresponding error bars. (b) Plot of emission intensity vs θ at λ = 565 nm utilizing the slot and the strip waveguides. Strong enhanced emission was found from the nanoslot waveguide at θ = 0° (TE mode).

sharply, as θ increased from 0 to 45°. In addition, the intensity versus θ plot apparently followed the sinusoidal variation, which can be explained by decomposing the linearly polarized waveguide mode into the orthogonal TE and TM components. The TE/TM ratio decreases, as θ increased from 0 to 45°. Here, the emission intensity when applying a strip waveguide was labeled by a dashed line, as shown in Figure 6b. Comparing the nanoslot waveguide to the strip waveguide, the sensitivity improvement due to the enhanced fluorescence was 9×. The result can be explained by the optical field enhancement found from the FDM modeling.

This sensitivity improvement was also observed from the fluorescence images captured during the measurements. When excited by the nanoslot waveguide shown in Figure 7a, the Cy3-labeled oligo created a strong fluorescence and bright yellow emission was found over the drop of analyte. After replacing the device by strip waveguides in Figure 7b, the fluorescence became less perceptible. Clearly, the nanoslot waveguide has a considerably higher fluorescence yield than the conventional strip waveguide. The device is functional across the entire temperature (RT ∼ 25 to 90 °C) and the pH (5−9) ranges of the DNA analyte stability, and the sensitivity improvement provided by the slot waveguide is independent of environmental parameters. Moreover, the sample volume
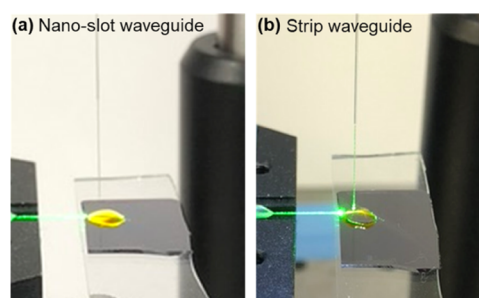

Figure 7. Fluorescence emitting from the oligonucleotide analyte excited by (a) nanoslot and (b) strip waveguide. Intensified fluorescence was observed when a nanoslot component was presented in the device.

actually used for performing the sensing was only 40 fL according to the geometry of the nanoslot fluidic channel (100 nm × 400 nm × 1 mm). On the other hand, standard viral detection methods, including PCR or the loop-mediated isothermal amplification (LAMP), relied on the amplification of the DNA copies. Both PCR and LAMP involve complex reagents to create target DNA concentrations ranging from 1 to 100 mg/mL. Nearly 10^9 copies per standard reaction volume of 0.1 mL was necessary to determine the detection of the DNA target. Clearly, our femtoliter nanoslot waveguide provided a highly accurate and small volume sensing platform for testing genetic samples. The cross-reactivity and selectivity of nucleic acid tests using the same N1 target as this work have been independently evaluated; findings suggest low prevalence of nucleotide mismatches and no cross-reactivity with human genome and microflora, other coronaviruses, and other respiratory viruses.[33,34] The nanoslot waveguide device can be further modified by specific biological receptors that provide the same selectivity and cross-sensitivity. For instance, through surface silanization, the slot waveguide can bond with various probe DNA molecules and trap their complementary single-stranded DNA, thus improving the selectivity of genetic molecule detection.

CONCLUSIONS

DNA sensors consisting of Si_3N_4 optofluidic waveguides were demonstrated for testing SARS-CoV-2 nucleic acid samples. Multiscale lithography followed by CMOS processes was used to create a 100 nm wide nanoslot waveguide structure. Polarization-dependent enhancement of the fluorescence emission was found upon testing the Cy3-tagged SARS-CoV-2 genetic material. The sensitivity improvement was due to the confinement of the excitation probe light within the nanofluidic channel. The slot waveguide sensing platform can be used with an extremely small sample volume suitable for remote detection of viral genetic materials.

AUTHOR INFORMATION

Corresponding Author

Pao Tai Lin − *Department of Electrical and Computer Engineering, Department of Materials Science and Engineering, and The Center for Remote Health Technologies and Systems, Texas A&M University, College Station 77843, Texas, United States;* orcid.org/0000-0002-5417-6920; Email: paolin@ece.tamu.edu

Author

Megan Makela − *Department of Electrical and Computer Engineering, Department of Materials Science and Engineering, and The Center for Remote Health Technologies and Systems, Texas A&M University, College Station 77843, Texas, United States;* orcid.org/0000-0002-3131-653X

Complete contact information is available at:
https://pubs.acs.org/10.1021/acs.analchem.0c02971

Author Contributions

M.M. conducted the experiments and data analysis. P.T.L. designed the optofluidic sensor devices and performed the FDM simulations.

Notes

The authors declare no competing financial interest.

■ REFERENCES

(1) Zhu, N.; Zhang, D.; Wang, W.; Li, X.; Yang, B.; Song, J.; Zhao, X.; Huang, B.; Shi, W.; Lu, R.; Niu, P.; Zhan, F.; Ma, X.; Wang, D.; Xu, W.; Wu, G.; Gao, G. F.; Tan, W.; China Novel Coronavirus Investigating and Research Team. *N. Engl. J. Med.* **2020**, *382*, 727−733.

(2) *Statement on the Second Meeting of the International Health Regulations (2005) Emergency Committee Regarding the Outbreak of Novel Coronavirus (2019-NCoV)*.

(3) *Coronavirus Disease (COVID-19); Situation Report 124*; World Health Organization, 2020.

(4) Fauci, A. S.; Morens, D. M. *N. Engl. J. Med.* **2016**, *374*, 601−604.

(5) Ebola Virus Disease in West Africa — The First 9 Months of the Epidemic and Forward Projections. *N. Engl. J. Med.* **2014**, *371* (), 1481−1495. DOI: 10.1056/NEJMoa1411100

(6) Neumann, G.; Noda, T.; Kawaoka, Y. *Nature* **2009**, *459*, 931−939.

(7) Parodi, S. M.; Liu, V. X. *JAMA* **2020**, *323*, 1441.

(8) Wang, C. J.; Ng, C. Y.; Brook, R. H. *JAMA* **2020**, *323*, 1341.

(9) Cheng, V. C. C.; Wong, S.-C.; Chen, J. H. K.; Yip, C. C. Y.; Chuang, V. W. M.; Tsang, O. T. Y.; Sridhar, S.; Chan, J. F. W.; Ho, P.-L.; Yuen, K.-Y. *Infect. Contr. Hosp. Epidemiol.* **2020**, *41*, 493−498.

(10) Corman, V. M.; Landt, O.; Kaiser, M.; Molenkamp, R.; Meijer, A.; Chu, D. K.; Bleicker, T.; Brünink, S.; Schneider, J.; Schmidt, M. L.; Mulders, D. G.; Haagmans, B. L.; van der Veer, B.; van den Brink, S.; Wijsman, L.; Goderski, G.; Romette, J.-L.; Ellis, J.; Zambon, M.; Peiris, M.; Goossens, H.; Reusken, C.; Koopmans, M. P.; Drosten, C. *Eurosurveillance* **2020**, *25*, 2000045.

(11) Chu, D. K. W.; Pan, Y.; Cheng, S. M. S.; Hui, K. P. Y.; Krishnan, P.; Liu, Y.; Ng, D. Y. M.; Wan, C. K. C.; Yang, P.; Wang, Q.; Peiris, M.; Poon, L. L. M. *Clin. Chem.* **2020**, *66*, 549−555.

(12) Mukundan, H.; Kumar, S.; Price, D. N.; Ray, S. M.; Lee, Y.-J.; Min, S.; Eum, S.; Kubicek-Sutherland, J.; Resnick, J. M.; Grace, W. K.; Anderson, A. S.; Hwang, S. H.; Cho, S. N.; Via, L. E.; Barry, C.; Sakamuri, R.; Swanson, B. I. *Tuberculosis* **2012**, *92*, 407−416.

(13) Luan, E.; Shoman, H.; Ratner, D.; Cheung, K.; Chrostowski, L. *Sensors* **2018**, *18*, 3519.

(14) Duveneck, G. L.; Pawlak, M.; Neuschaefer, D.; Budach, W.; Ehrat, M. Novel Generation of Luminescence-Based Biosensors: Single-Mode Planar Waveguide Sensors. In *Biomedical Systems and Technologies*; International Society for Optics and Photonics, 1996; Vol. *2928*, pp 98−109.

(15) Rong, G.; Najmaie, A.; Sipe, J. E.; Weiss, S. M. *Biosens. Bioelectron.* **2008**, *23*, 1572−1576.

(16) Lin, P. T.; Singh, V.; Wang, J.; Lin, H.; Hu, J.; Richardson, K.; Musgraves, J. D.; Luzinov, I.; Hensley, J.; Kimerling, L. C.; Agarwal, A. *Opt. Mater. Express* **2013**, *3*, 1474−1487.

(17) Lin, P. T.; Singh, V.; Lin, H.-Y. G.; Tiwald, T.; Kimerling, L. C.; Agarwal, A. M. *Adv. Opt. Mater.* **2013**, *1*, 732−739.

(18) Schmidt, H.; Hawkins, A. R. *Nat. Photonics* **2011**, *5*, 598−604.

(19) Lin, P. T.; Kwok, S. W.; Lin, H.-Y. G.; Singh, V.; Kimerling, L. C.; Whitesides, G. M.; Agarwal, A. *Nano Lett.* **2014**, *14*, 231−238.

(20) Yang, A. H. J.; Moore, S. D.; Schmidt, B. S.; Klug, M.; Lipson, M.; Erickson, D. *Nature* **2009**, *457*, 71−75.

(21) Snow, R. W.; Guerra, C. A.; Noor, A. M.; Myint, H. Y.; Hay, S. I. *Nature* **2005**, *434*, 214−217.

(22) Bhatt, S.; Gething, P. W.; Brady, O. J.; Messina, J. P.; Farlow, A. W.; Moyes, C. L.; Drake, J. M.; Brownstein, J. S.; Hoen, A. G.; Sankoh, O.; Myers, M. F.; George, D. B.; Jaenisch, T.; Wint, G. R. W.; Simmons, C. P.; Scott, T. W.; Farrar, J. J.; Hay, S. I. *Nature* **2013**, *496*, 504−507.

(23) Ferrari, M. J.; Grais, R. F.; Bharti, N.; Conlan, A. J. K.; Bjørnstad, O. N.; Wolfson, L. J.; Guerin, P. J.; Djibo, A.; Grenfell, B. T. *Nature* **2008**, *451*, 679−684.

(24) Sacher, W. D.; Luo, X.; Yang, Y.; Chen, F.-D.; Lordello, T.; Mak, J. C. C.; Liu, X.; Hu, T.; Xue, T.; Guo-Qiang Lo, P.; Roukes, M. L.; Poon, J. K. S. *Opt. Express* **2019**, *27*, 37400−37418.

(25) Gorin, A.; Jaouad, A.; Grondin, E.; Aimez, V.; Charette, P. *Opt. Express* **2008**, *16*, 13509−13516.

(26) Alasaarela, T.; Korn, D.; Alloatti, L.; Säynätjoki, A.; Tervonen, A.; Palmer, R.; Leuthold, J.; Freude, W.; Honkanen, S. *Opt. Express* **2011**, *19*, 11529−11538.

(27) Debnath, K.; Khokhar, A. Z.; Boden, S. A.; Arimoto, H.; Oo, S. Z.; Chong, H. M. H.; Reed, G. T.; Saito, S. Low-Loss Slot Waveguides with Silicon (111) Surfaces Realized Using Anisotropic Wet Etching. *Front. Mater. Sci.* **2016**, *3*. DOI: 10.3389/fmats.2016.00051

(28) CDC. Information for Laboratories about Coronavirus (COVID-19) https://www.cdc.gov/coronavirus/2019-ncov/lab/rt-pcr-panel-primer-probes.html (accessed Nov 19, 2020).

(29) Health, C. for D. and R. Emergency Use Authorizations for Medical Devices https://www.fda.gov/medical-devices/emergency-situations-medical-devices/emergency-use-authorizations-medical-devices (accessed Nov 19, 2020).

(30) Deng, Q.; Liu, L.; Li, X.; Zhou, Z. *Opt. Lett.* **2014**, *39*, 5665−5668.

(31) Butt, M. A.; Khonina, S. N.; Kazanskiy, N. L. *Appl. Opt.* **2020**, *59*, 7821−7828.

(32) Sanborn, M. E.; Connolly, B. K.; Gurunathan, K.; Levitus, M. *J. Phys. Chem. B* **2007**, *111*, 11064−11074.

(33) Lu, X.; Wang, L.; Sakthivel, S. K.; Whitaker, B.; Murray, J.; Kamili, S.; Lynch, B.; Malapati, L.; Burke, S. A.; Harcourt, J.; Tamin, A.; Thornburg, N. J.; Villanueva, J. M.; Lindstrom, S. US CDC Real-Time Reverse Transcription PCR Panel for Detection of Severe Acute Respiratory Syndrome Coronavirus 2, *Emerging Infect. Dis.*, **2020**, *26* (). DOI: 10.3201/eid2608.201246.

(34) Vogels, C. B. F.; Brito, A. F.; Wyllie, A. L.; Fauver, J. R.; Ott, I. M.; Kalinich, C. C.; Petrone, M. E.; Casanovas-Massana, A.; Catherine Muenker, M.; Moore, A. J.; Klein, J.; Lu, P.; Lu-Culligan, A.; Jiang, X.; Kim, D. J.; Kudo, E.; Mao, T.; Moriyama, M.; Oh, J. E.; Park, A.; Silva, J.; Song, E.; Takahashi, T.; Taura, M.; Tokuyama, M.; Venkataraman, A.; Weizman, O.-E.; Wong, P.; Yang, Y.; Cheemarla, N. R.; White, E. B.; Lapidus, S.; Earnest, R.; Geng, B.; Vijayakumar, P.; Odio, C.; Fournier, J.; Bermejo, S.; Farhadian, S.; Dela Cruz, C. S.; Iwasaki, A.; Ko, A. I.; Landry, M. L.; Foxman, E. F.; Grubaugh, N. D. *Nat. Microbiol.* **2020**, *5*, 1299−1305.